PERGAMON

International Journal of Heat and Mass Transfer 44 (2001) 3755–3764

International Journal of HEAT and MASS TRANSFER

www.elsevier.com/locate/ijhmt

Holographic interferometry applied to coupled free convection and radiative transfer in a cavity containing a vertical plate between 290 and 650 K

E. Lacona, J. Taine *

Laboratoire EM2C de l'ECP et du CNRS (UPR 288), École Centrale Paris, 92295 Châtenay-Malabry Cedex, France

Received 3 April 2000

Abstract

Holographic interferometry has been applied, in the presence of strong beam deflection effects, to the study of the coupling of gas–gas radiative transfer and free convection in a 0.9 m^3, isothermal, gastight cavity containing an isothermal plate of finite thickness and filled with N_2 or CO_2. The cavity is heated in the range 290–650 K with the plate at a higher temperature. The focus of this paper is on the validation of an original experimental procedure for the determination of thermal fields in the region close to the plate. Experimental results agree both with independent experimental results using a laser beam deflection technique and, in case of pure free convection, with classical bibliography results related to a vertical wall. It has been shown that gas–gas radiative transfer significantly modifies the temperature field corresponding to free convection and increases the local heat transfer coefficient.

1. Introduction

Accurate experimental determinations of the temperature fields in a gas by intrusive classical techniques are difficult to implement when radiative transfer significantly contributes to the thermal balance of the sensor. Furthermore, in the case of an absorbing and emitting gas, the complex intensity field, incident on the sensor, has also to be accounted for. For instance, thin thermocouples equipped with radiative shields have been successfully used in the core of a strong forced CO_2 flow [1]. Such a technique is inappropriate to study the boundary layers in the case considered here of free convection coupled to radiation. In this case, the heat transfer coefficient on the sensor would be smaller than previously and the shield would strongly perturb the boundary layer. In practice, optical techniques, which are not intrusive, are required in this type of application. Diverse optical techniques can be implemented, such as spectroscopic methods [1], Raman scattering [2,3], Rayleigh scattering [4] and LIF methods [5], speckle method [6], laser beam deflection method [7–11] and interferometric methods [12–17].

The present study deals with two techniques based on the determination of the refraction index field, principally holographic interferometry, but also the laser beam deflection technique, considered as reference. Diverse physical quantities have been measured by the last method, such as thermal diffusivity [7], gas density [8], etc. Zhang et al. [9] and other authors [10,11] have also determined temperature fields and local heat transfer coefficients in the case of pure free convection or radiative transfer coupled to laminar or turbulent forced convection. Holographic interferometry is much more complex to implement than the deflection technique. However, it allows a direct whole field record, instead of a large number of point-by-point measurements. A general theory has been given in [17] and a detailed description of different techniques can be found in [14]. The holographic interferometry method has been

* Corresponding author. Tel.: +33-1-41-13-10-63; fax: +33-1-47-02-80-35.

E-mail address: taine@em2c.ecp.fr (J. Taine).

0017-9310/01/$ - see front matter
PII: S0017-9310(01)00027-8

Nomenclature

a	polynom coefficients expressing temperature
D_x, D_y	horizontal and vertical sensor center displacements (mm)
e	plate width (m)
e_x, e_y	horizontal and vertical distances of the spot center (mm)
f	frequency (Hz)
Gr_x	local Grashof number
h	local heat transfer coefficient (W/(m^2 K))
H	plate height (m)
K	Gladstone–Dale constant (K^{-1})
L	plate length (m)
L_i	optical path (m)
n	refractive index
Pr	Prandtl number
Ra_x	local Rayleigh number
T_c	cavity temperature (K)
T_p	plate temperature (K)
T_0	mean temperature (K)
x_0, y_0	beam entrance coordinates (m)
y_S	beam plate exit position (m)
α_v	equivalent absorptivity
δ_x, δ_y	horizontal and vertical sensor displacements (mm)
$\delta(x)$	boundary layer thickness (m)
$\Delta(t)$	time (s)
ϵ	constant
ϵ_σ	variance
λ	gas thermal conductivity (W/(m K))
λ	wavelength (m)
σ	optimization criterion
$\theta(x^+, y^+)$	dimensionless temperature

applied to heat and mass transfer by Mayinger [15]. Hwang and Liou [16] have measured the heat transfer coefficients in an air flow in a rectangular chamber with turbulence promoters. Recently, Herman et al. [12,13] have visualized unsteady phenomena in complex geometries and Bdéoui [18] has qualitatively investigated the temperature distribution in a rectangular enclosure in order to study the coupling of Rayleigh–Bénard convection and radiative transfer.

The present work is the first experimental step towards the study of long-range effects of gas–gas radiation on thermal fields in a gas flowing by free convection around an actual finite plate, i.e., of finite thickness, included in a cavity. Many works deal with the coupling between free convection and radiation [19–22]. However, to the best of our knowledge, there is a lack of data related to the previously defined problem, excluding the recent numerical work of Foucher and Petit [23]. A large-sized gastight cavity has been designed and built in order to obtain, in the first step, local free-field conditions on a part of the vertical plate walls. In this manner the experimental results can also be compared to classical data related to this configuration. However, a consequence of this design choice is that the thermal conditions required by implemented experimental techniques are close to the conditions of transition to chaos in the flow. Section 2 deals with the design of the cavity, its thermal control and the visualization window system. The laser beam deflection technique is summarized in Section 3.1 and the implementation and original evaluation procedure of the holographic interferometry setup are described in Section 3.2. Experimental results are validated and discussed in Section 4.

2. Experimental cell

The structure and dimensions of the experimental cell are shown in Fig. 1. It is a parallelepipedic cavity, 0.9 m high, of square basis of 1 m edge, enclosed in a 2 m diameter gastight tank. Each cavity wall is made of two copper plates, 1 cm thick. The low mechanical resistance of copper at high temperature requires to make these walls rigid with a steel structure. The cavity is also externally insulated by rockwool layers, 10 cm thick and of thermal conductivity 0.082 W m^{-1} K^{-1}. A square copper plate ($L = 30$ cm, $H = 30$ cm and $e = 3$ cm) is hung on top of the tank and is precisely positioned in the cavity center.

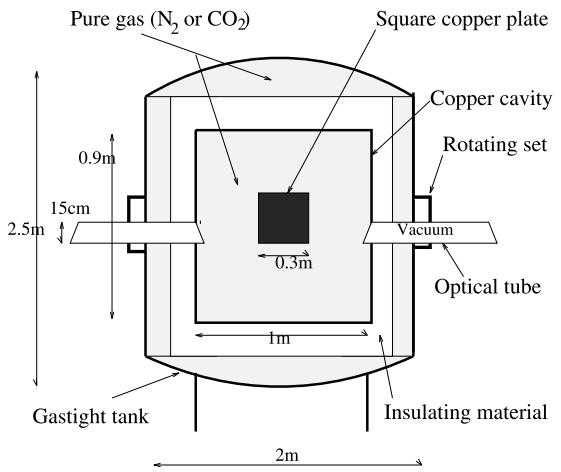

Fig. 1. Experimental cell: schematic cross-section.

The temperatures T_p and T_c, of both the plate and the cavity walls may be regulated to values as high as 650 and 590 K, respectively. Fig. 2 shows the layout of the heaters and the thermocouples for a vertical cavity wall and the plate. In the first case, a good contact between the heaters and the copper cavity walls is accomplished by the rigid steel structure. The internal plate is made of two 1 cm thick copper plates which press flat heaters and other copper plates. The temperatures are measured by "Chromel–Alumel" thermocouples, of 1 mm diameter, insulated from ground. They are carefully embedded, perpendicular to the walls, at 1 mm of the internal face of the walls. All temperature values are transferred to an "AIOP" computer. Fifteen independent "Vulcanic" control systems maintain isothermal conditions in the cavity walls. For high temperature conditions, a steady state is reached in the cavity in about 48 h. Due to the large size of this cavity, temperature differences are typically of the order of 0.5–2 K and less than 4 K in extreme conditions. For the plate, isothermal conditions are obtained by three independent "Eurotherm" control systems with an accuracy close to the temperature measurement accuracy (some 0.1 K).

The whole tank and consequently the cell are filled with pure N_2 (N50) or CO_2 (N48), from "Air Liquide". A basic vacuum (of about 100 Pa) is first made and the tank is filled. This procedure is repeated three or four times. The tank pressure is always controlled at a value higher than the atmospheric pressure in order to minimize O_2 and H_2O molar fractions in the tank and avoid wall oxidation.

Two optical tubes, of 15 cm diameter, cross the tank and are settled out in the middle of two opposed vertical cavity walls in order to allow visualization around the plate. One of them is shown in Fig. 3. Silica and quartz "Heraeus" windows, 15 mm thick, tilted with a 5° angle in order to prevent multiple reflection effects, close the external and internal optical tube extremities, respectively. The internal part of the tube is heated at the cavity temperature, while the external part is cooled at room temperature by a water flow. During the experiment, the optical tubes remain under a primary vacuum (about 1 Pa) in order to eliminate any deflection effect and to minimize thermal losses, which are then mainly

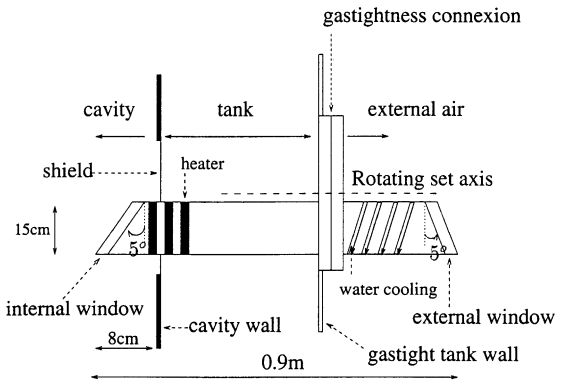

Fig. 3. Optical tube (the tilted angle of the internal and external windows has been exaggerated).

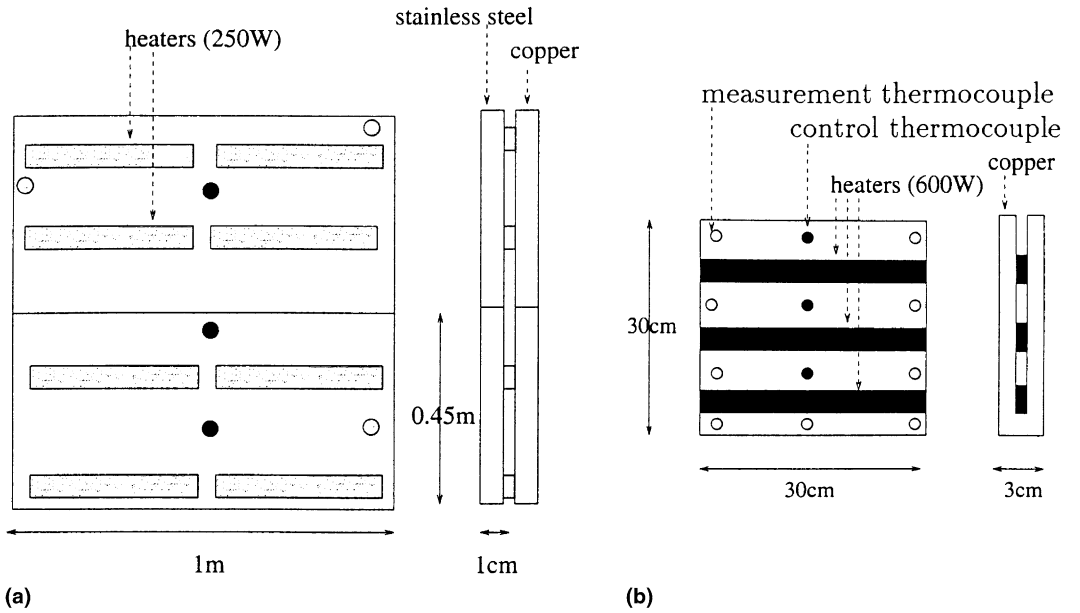

Fig. 2. (a) Thermal control of a cavity wall. (b) Thermal control of the vertical plate. The control thermocouples are connected to the thermal control system and the measurement thermocouples allow checking the isothermal conditions in the cavity and on the plate.

radiative through the tube extremities. The tube axis does not coincide with the rotating set axis, in order to allow visualization of a 40 cm diameter region corresponding to different tube positions from bottom to top. "Viton" seals allow the cell and tube gastightness, at a temperature as high as 430 K both under pressure and vacuum conditions. Connections allow pressure measurements, gas feeding and vacuum.

3. Optical setup and procedures

Both the holographic interferometry and laser beam deflection setups are mounted over two optical tables lying on the same original, rigid and horizontal 2 m × 5 m "Kinetic System" structure. The whole structure is controlled by a pneumatic master–slave system and is insulated from external vibrations. Its rigidity and the weight of tables ensure a very good flatness and the stability required by the holographic interferometry technique. The two optical setups are independent and a technique can be used without modifying the optical elements of the other one.

3.1. Laser beam deflection

The laser beam deflection method relies on the fact that a beam crossing a medium of nonhomogeneous refractive index field $\boldsymbol{n}(\boldsymbol{r})$ is deflected towards the stronger index value region. The resulting displacement depends, at constant pressure, on the temperature field. The complete optical setup and exploitation procedure in use here have been validated by Zhang et al. [9] and El Ammouri and Taine [10] at a small scale. For a laminar natural convection flow in air along a vertical isothermal plate, the Nusselt number determined by this technique and corresponding bibliographic data agree with a relative accuracy of about 0.01–0.02 [9].

The light source is a He–Ne laser of 2 mW. A motorized unit, including a step-by-step motor, allows precise horizontal displacements of the beam with a spatial resolution of about 10 μm. The laser beam, initially horizontal and parallel to the plate, is focused in the middle of this plate in order to minimize its size in the interaction region. After deflection along the plate towards the colder region (see Fig. 4), the beam is collected by a diode position sensor "SDC-386-22-21-251", located 4.7 m away from the plate exit edge. The sensor is characterized by an active surface of 10 mm × 10 mm. After natural expansion, the laser spot diameter on the sensor is about 8 mm. This sensor in mounted on two step-by-step motorized units, used in such a manner that the spot center is always close to the sensor center in order to get an optimal response linearity. The sensor gives two electrical voltages which correspond to the horizontal and vertical distances of the spot center to the sensor center (e_x, e_y). For each entrance laser beam position (x_0, y_0), the sensor center displacements D_x and D_y are also recorded and consequently the total beam displacements $\delta_x = D_x + e_x$ and $\delta_y = D_y + e_y$. All the displacements of the step-by-step motors are controlled by a computer (Commodore 1930) which also performs the acquisition of the laser beam displacements.

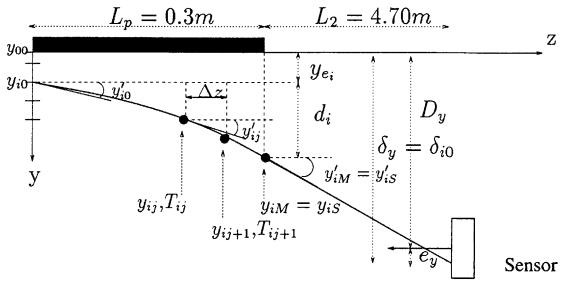

Fig. 4. Deflected beam discretization at a position x_0 in the plane Oyz (the deflection angle and the displacement have been exaggerated).

Optical adjustments are detailed in [24]. We consider now only 1D trajectories in the plane Oyz, as shown in Fig. 4. In entrance, y_0 values are discretized by steps of 0.2 mm in the range 0.8–5 mm, and by steps of 1 mm in the range 5–16 mm. In practice, for each entrance position x_0, the displacements δ_{i0} associated with y_{i0} are averaged during a time Δt $(1 - 3s)$, with a sampling frequency f (100–500 Hz). Each displacement function $\delta_{i0}(y_{i0})$ is an average of different results. It is worth noting that, in practice, displacements are measured by reference to the beam positions corresponding to experiments with all the system at the cavity temperature. This approach is discussed in [9]. As a result, the laser beam translation, occurring when going through the optical windows of large thickness, is eliminated.

The temperature fields are extracted from the experimental displacement fields by a parameter estimation method. This method has been validated and its accuracy is discussed by Zhang et al. [9].

3.2. Holographic interferometry

3.2.1. Optical setup and procedure

The holographic interferometry setup is shown in Fig. 5. The helium–neon laser beam (L: 0.95 mW) crosses a shutter O and is divided by a variable beam splitter S into two equal intensity parts. A reference beam propagates outside the experimental cell. It is expanded and spatially filtered (L_{mr}). The expanded beam is transformed into a planar wave by a 15 cm diameter lens (L_r). The main beam, after being expanded, filtered (L_{mo}) and collimated (L_o), propagates in the cavity along the experimental plate. The set of mirrors (M1–M2–M3) allows to equalize the two optical paths.

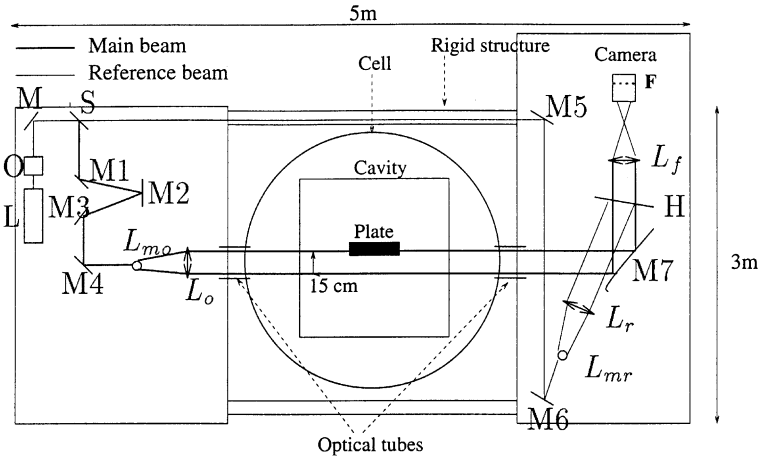

Fig. 5. Holographic interferometry optical setup. L: laser; O: shutter; S: beam splitter; L_{mo}, L_{mr}: sets of an objective and a pinhole (15 μm); L_o, L_r: lens ($D = 150$ mm, $f = 300$ mm); M, M1, M2, M3, M4, M5, M6: plane mirrors ($D = 50$ mm); M7: plane mirror ($D = 300$ mm); L_f: lens ($D = 150$ mm, $f = 450$ mm); H: holographic plate; F: camera film.

In the first step (hologram recording), the experimental plate is at the cavity temperature (reference state). The expanded reference and main beams interfere, on the holographic photographic plate "Kodak" H, which is exposed for 500 ms. After processing, the holographic plate is replaced as precisely as allowed by the plate holder. In ideal conditions, the object wave, reconstructed by the reference beam going through the hologram, in the main beam direction, is proportional to the wave issued of the main beam. As a result no fringes appear when the main beam is added. In practice, the holographic plate is not precisely replaced, small temperature variations occur in the cell or in the room, and small optical displacements can appear. These uncontrolled phenomena generate undesired fringes. By adjusting the lens L_o, it is possible to strongly attenuate these fringes.

The residual fringes are large enough to be distinguished from studied fringes. An alternative way would be to process directly the holographic plate on the holder, as done by Mayinger and Panknin [25], who had positioned the plate in a cell filled with water during the exposure time. In that case, a small temperature gradient in the cell also generates perturbations.

In a second step, the experimental plate in the test cell is heated and a refractive index field is changed by the local temperature field. After steady state has been reached in the cell, the holographic plate is illuminated both by the main beam, perturbed by the new refractive index field, and the reference beam. The fringes to study appear in the boundary layer image. The interference fringes are recorded on the film of a camera without an objective lens in the image plane conjugated by the lens L_f. From an optical point of view, the lens L_f selects an object plane, in which the phenomenon is studied, and associates to it an observation image plane (film plane). As a real object would perturb the gas flow, a complementary optical setup shown in Fig. 6 has been used. An image I_1 of a real plane object O_1 (graduated target) is formed in the selected object plane O_2. A sharp image of I_1 (or O_2) is then obtained by the lens L_f in the film (F). The object O_1 also acts as a reference length scale, needed by any quantitative evaluation of the interference fringes. The superposition of an image of fringes and of an image of O_1 allows accurate conversions into metric units.

The use of a black and white photographic film is due to its excellent resolution in steady-state conditions. The image is then scanned and digitalized in a matrix of 100 pixels/mm and 256 gray levels.

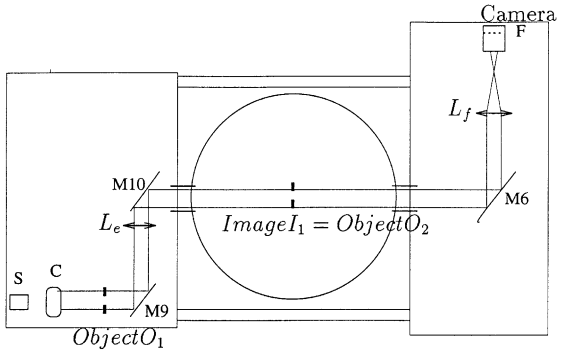

Fig. 6. Image sizing setup. S: white light source; C: condensor; L_e: lens ($D = 100$ mm, $f = 1000$ mm); M9, M10: plane mirrors ($D = 300$ mm).

3.2.2. Image processing and interferogram evaluation

Fig. 7(a) shows an image related to an experiment with N_2 at $T_c = 270°C$; $T_p = 330°C$. The white part of the image corresponds to a 2 cm width and 5 cm high area of the plate. Fig. 7(b) shows an example of intensity profile along a line perpendicular to the vertical wall, at the distance $x_0 = 20$ mm from the plate bottom. Intensity profile maxima and minima correspond to the fringe positions. As the profiles are noisy, they are adjusted by a least-square minimization procedure around each extremum. The apparent wall position is assumed to correspond to the middle position between the wall (gray level = 240) and the profile axis. A conventional interpretation of interferograms is based on the assumption of straight line light propagation, i.e., each fringe corresponds to an iso-refractive index line or an isotherm at constant pressure. The knowledge of one absolute temperature (plate or cavity) and of the temperature difference between two fringes, from the Gladstone–Dale law [26], leads to the whole temperature field along a line. However, in our conditions, beam deflections due to temperature gradients are important and the expanded laser beam, entering the thermal boundary layer in the immediate vicinity of the heated plate, is deflected towards the gas by more than 0.2 mm at the end of the plate. Consequently, the plate exit plane is chosen as the object plane O_2 of Fig. 6. Indeed, according to this choice, the fringe positions in the film plane F allow, by applying a simple magnification law, to characterize equiphase points in the object plane O_2 and, in a second step, an associated trajectory along the plate. Fig. 8 presents beam trajectories along the plate leading to fringes in the observation plane. In this way, the apparent plate wall is displaced by y_{0S}.

Different problems have to be solved in order to determine the gas temperature field: (i) the distance y_{0S} of the apparent wall position to the actual one is unknown; (ii) the only quantitative information related to the temperature field is the phase difference between consecutive fringes, which depends on both the exact lengths of the trajectories in the interaction region and the crossed index field [27]. Consequently, all the beam trajectories corresponding to the observed fringes, called i, have to be determined. They are experimentally defined by both an entrance angle y_0', measured and controlled for each experiment, and the distance to the apparent wall position in the object plane O_2, $y_{iS} - y_{0S}$ (see Fig. 8). The dimensionless temperature profile along

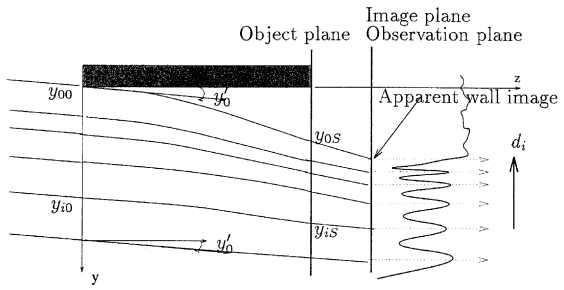

Fig. 8. Fringe positions in the observation plane and beam trajectories corresponding to these positions.

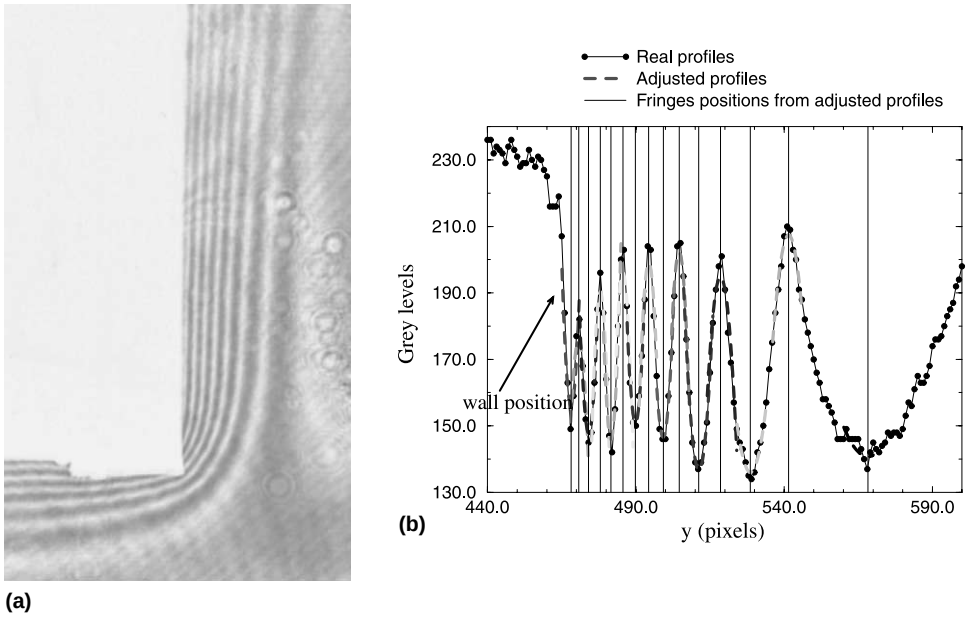

Fig. 7. (a) Experiment with N_2: $T_c = 270°C$; $T_p = 330°C$; $p = 1.15 \times 10^5$ Pa. (b) Profiles at $x_0 = 20$ mm from the plate bottom.

a line $\theta(x_0, y^+)$ is expressed as a given function depending on P parameters, i.e.,

$$\theta(x_0, y^+) = \frac{T(y) - T_c}{T_p - T_c} = 1 + \sum_{j=1}^{P} a_j (y^+)^j. \quad (1)$$

In Eq. (1), y^+ is given by $y^+ = y/E$ where y is the distance to the wall, and E the thickness of the region in which fringes are evaluated. Two supplementary boundary conditions in $y^+ = 1$ are considered:

$$\theta(x_0, 1) = 0 \quad \text{or} \quad 1 + \sum_{j=1}^{P} a_j = 0, \quad (2)$$

and

$$\frac{d\theta}{dy^+}(x_0, 1) = 0 \quad \text{or} \quad \sum_{j=1}^{P} j a_j = 0. \quad (3)$$

Consequently $Q = P - 2$ parameters are unknown. $\theta(x_0, y^+)$ is determined from an original iterative parameter estimation method, based on a sequential simplex search [28]. At each iteration, a parameter vector $A_j = (a_1, a_2, \ldots, a_P)$ is used and we calculate: (i) the apparent wall position y_{0S} in the object plane O_2, and its antecedent y_{00} in the entry plane, (ii) the whole trajectories which lead to the equiphase points i, which are characterized both by y_0' and by the distance d_i defined in Fig. 8. This allows to calculate $y_{iS} - y_{i0}$ in the object plane O_2, i.e., in a discretized form (see Fig. 4) as

$$y_{iS} - y_{i0} = \left(\sum_{j=0}^{M-1} y_{ij}'' \right) \frac{\Delta z^2}{2} + M y_0' \Delta z + \left(\sum_{j=0}^{M-1} \sum_{k=0}^{j-1} y_{jk}'' \right) \Delta z^2, \quad (4)$$

where $y_{ij}'' = -K/T_{ij}^2 (dT/dy)_{ij}$ is calculated at the point j of the considered trajectory i. More details are given in [24]. The optical path difference $L_i - L_{i-1}$ associated with two consecutive dark and bright fringes (and consecutive trajectories) can then be calculated, from the expression

$$L_i = \sum_{j=0}^{M} \left(1 - \frac{K}{T_{ij}} \right) \frac{\Delta z}{\cos[(y_{ij+1} - y_{ij})/\Delta z]} \quad (5)$$

of which the discretization is defined in Fig. 4. The method is based on the minimization of σ, defined by

$$\sigma_k = \sqrt{\frac{1}{N} \sum_{i=1}^{N} \left[\frac{(L_{ik} - L_{(i-1)k})}{\lambda/2} - 1 \right]^2}, \quad (6)$$

where L_{ik} is the optical path at the iteration k, associated with the fringe i. For Q parameters to be determined, $Q + 1$ vectors A_k are first introduced and the iterative procedure is repeated, by changing the worst vector at each step, as explained in [9,28]. The iteration continues until one of the two following criteria is satisfied: (i) a physical convergence criterion, defined by

$$\sigma_k < \epsilon_\sigma \Delta L_{max}, \quad (7)$$

where ϵ_σ is the estimated variance of the experimental relative error on the optical path and ΔL_{max} is the maximum optical path difference, (ii) a mathematical criterion, defined by

$$\sqrt{\frac{1}{Q+1} \sum_{k=1}^{Q+1} (\sigma_k - \langle \sigma \rangle)^2} < \epsilon \langle \sigma \rangle, \quad (8)$$

where

$$\langle \sigma \rangle = \frac{1}{Q+1} \sum_{k=1}^{Q+1} \sigma_k, \quad (9)$$

where ϵ is an arbitrary small value. No other adjustment of A would lead to further improvement. In practice, we have chosen $P = 3$, as widely discussed in [24], and used as initial temperature profile the temperature field obtained using the conventional approach.

Sensibility analyses of the evaluation methods [24] have shown that, for given theoretical temperature fields, the coefficient a_1 is determined with an accuracy of about 0.5% for holographic interferometry with $P = 3$ and $\sigma = 0.0002$, and about 0.8% for the laser beam deflection, with $P = 5$ and $\sigma = 0.0001$. In weak noisy experiments, the accuracy related to the determination of the local heat transfer coefficient is then about a few percent.

4. Results and discussion

The considered temperature range is 290–650 K and three temperature differences between the plate and the cavity are chosen in the range 15–60 K in such a manner that the fringe number is sufficient for the interferogram exploitation. In practice, taking into account the film and the scanner resolutions, the optimum number of fringes is of the order of 7–12. The optical tubes have been positioned to allow visualization of the plate bottom region. Fringe profiles have been treated both for horizontal lines close to the vertical wall ($x_0 = 5,\ 10,\ 20,\ 30,\ 40,\ 50$ mm) and for vertical lines close to the horizontal wall ($y_0 = 5,\ 10,\ 15$ mm).

4.1. Nonabsorbing gas

Experiments related to N_2 have been carried out to validate both the experimental setup and the exploitation procedure by comparison with experimental results of the laser beam deflection technique, previously validated in rather similar conditions [9]. Furthermore, the

cell has been built in order to obtain in the vertical wall region, not too close to the edge, conditions of free field type. Experimental results can then also be compared to a classical solution of an isothermal plate in a free field, with a temperature field simply given by [29]

$$T(x,y) = T_c + (T_p - T_c)(1 - y/\delta(x))^2, \tag{10}$$

where $\delta(x)$ is the boundary layer thickness, expressed as

$$\delta(x) = 3.93\,Pr^{-0.5}(0.952 + Pr)^{1/4} Gr_x^{-1/4} x. \tag{11}$$

The Prandtl and the local Grashof and Rayleigh numbers Pr, Gr_x and Ra_x are calculated with thermophysical properties taken at the temperature $T_0 = (T_p + T_c)/2$. The theoretical local heat transfer coefficient is given by [30]

$$h_x = \lambda(T_p)0.503[Pr/(Pr + 0.986Pr^{1/2} + 0.492)]^{1/4} Ra_x^{-1/4} x^{-1}, \tag{12}$$

where $\lambda(T_p)$ is the thermal gas conductivity, taken at wall temperature. The experimental expression of the local heat transfer coefficient is, for the vertical wall

$$h_x^{exp} = -\frac{\lambda(T_p)}{T_p - T_c}\left(\frac{\partial T}{\partial y}\right)_{y=0}^{exp}(x). \tag{13}$$

Fig. 9 shows typical examples of temperature profiles close to the vertical wall, issued from both optical methods, at $T_c = 270°C$, $T_p = 330°C$. A typical dependence of the local heat transfer coefficient vs x, at ambient temperature ($T_c = 20°C$, $T_p = 50°C$) is shown in Fig. 10. Experimental points are issued from different experiments in the same conditions. In both cases, a good agreement is obtained. It is worth noting that, in our conditions, the holographic interferometry technique cannot be used as far in the boundary layer as the laser beam deflection technique, due to the presence of unwanted large-sized fringes, resulting from the holographic plate repositioning. Relative differences between experimental and calculated local heat transfer coefficients are, for $x_0 > 10$ mm, about 0.03 at ambient temperature and less than 0.05 at higher temperature. Stronger differences around the leading edge are due to the fluid pre-heating, along the horizontal boundary layer. As a result the experimental local heat transfer coefficient is smaller than the theoretical one.

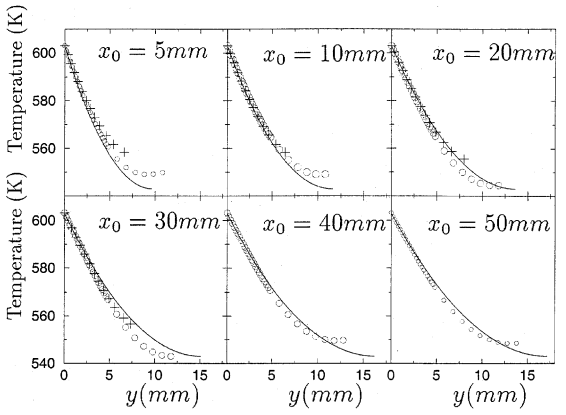

Fig. 9. Calculated and experimental temperature profiles. Experiments with N_2: $T_c = 270°C$; $T_p = 330°C$; $p = 1.15 \times 10^5$ Pa; $y_0' = 0.003$ rad; (—) calculation; (+) holographic interferometry; (○) laser beam deflection.

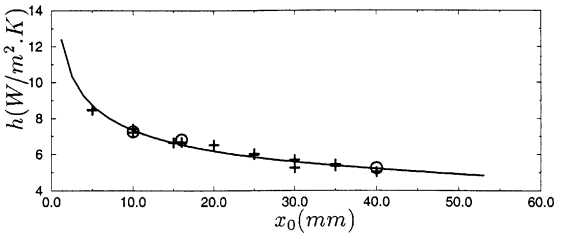

Fig. 10. Local heat transfer coefficient vs x_0. Experiments with N_2: $T_c = 20°C$; $T_p = 50°C$; $p = 1.14 \times 10^5$ Pa; $y_0' = 0.003$ rad; (—) calculation; (+) holographic interferometry; (○) laser beam deflection.

Examples shown before and all other obtained results validate both the experimental setups and the original exploitation technique. An exploitation of interferograms, without taking into account the beam deflection effect, has led to a relative overestimation of about 0.1 of the local heat transfer coefficient.

4.2. Absorbing gas

Experiments at high temperature related to pure CO_2 (at pressure close to atmospheric pressure) are now considered. The temperature horizontal profiles vs y, close to the vertical wall, obtained by the two optical techniques are in good agreement [24].

Fig. 11 shows, for different temperature conditions, typical results for the local heat transfer coefficient, related to the wall conductive flux coupled both to gas–gas radiation and free convection. Experimental results are more dispersed in the case of CO_2 than in the case of N_2. This phenomenon is due to the fact that the required experimental thermal conditions correspond to the limit of instable flow occurence, which appears in CO_2 for smaller Grashof numbers than in N_2, as pointed by Bdéoui [31].

A comparison is also made with the free field purely convective model which considers CO_2 as a transparent species. In the chosen conditions, the corresponding boundary layer thickness would be smaller than that associated with N_2, and the flow would be a fortiori in free field conditions. At ambient temperature, the experimental coupled heat transfer coefficient agrees with the calculated purely convective one. The effect of

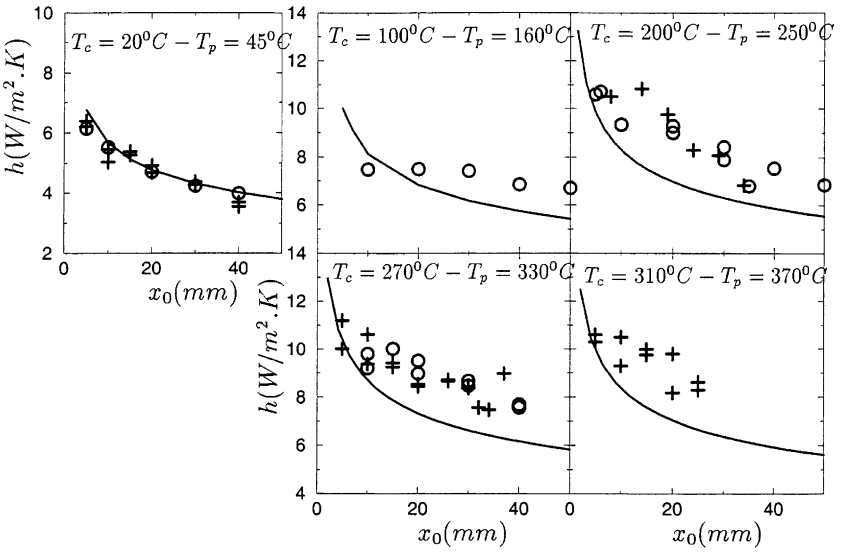

Fig. 11. Local heat transfer coefficient vs x_0, for different temperature conditions. Experiments with CO_2: $p = 1.10 \times 10^5$ Pa; $y_0' = 0.003$ rad; (—) calculation without radiation; (+) holographic interferometry; (○) laser beam deflection.

coupling is then negligible. For $x_0 > 10$ mm, as the temperature increases, the experimental local heat transfer coefficient becomes higher than the calculated one. Along the plate, the contribution of gas–gas radiation to the local heat transfer coefficient can be roughly estimated as

$$h^R = \left[\int_v \alpha_v(\delta)\pi[I_v^o(T_0) - I_v^o(T_c)]\,dv\right] \Big/ (T_p - T_c), \qquad (14)$$

where $\alpha_v(\delta)$ is the equivalent absorptivity of the whole boundary layer at the mean temperature T_0, and I_v^o is the equilibrium intensity. Taking into account the large size of the cell, filled with pure CO_2 (at $p = 1.12 \times 10^5$ Pa) which has strong absorption bands, the gas in the cavity is crudely considered as a black body in the absorption bands. The quantity defined by Eq. (14) remains practically constant vs x, due to the weak δ variation in the range 10–40 mm, and approximately corresponds to the difference between the theoretical curves of Fig. 11 and the experimental points. Close to the leading edge, the experimental local heat transfer coefficient is equal to or smaller than the calculated one. Indeed, the gas has also been pre-heated by convection, along the horizontal boundary layer, and by radiation, at a distance. A coupled modeling of free convection and radiation has been carried out in the considered experimental conditions [24]. The thermal and geometry conditions corresponding to an unstable flow solution, the convergence of the convection problem have not been reached. Results related to the local heat transfer coefficient at the horizontal bottom wall, at low and high temperatures, in both N_2 and CO_2 have also been reported in [24].

5. Conclusion

In this first work, a large-sized, gastight, experimental cell has been built and can be regulated up to 650 K. The holographic interferometry setup and its original exploitation technique have been validated. First results related to coupled gas radiation and free convection have been obtained. The next experimental step will deal with the determination of the 2D temperature field in the region close to the edge, taking into account the strong 2D effects of the beam deflection in the interferograms.

References

[1] A. Soufiani, J. Taine, High-resolution spectroscopy temperature measurements in laminar channel flows, Appl. Opt. 27 (17) (1988) 3754–3760.
[2] W. Stricker, Local temperature measurements in flames by laser Raman spectroscopy, Combust. Flames 27 (1976) 133–136.
[3] D. Ball, R.J. Driver, R.D. Hutcheon, R.D. Lockett, G.D. Robertson, Coherent anti-Stokes Raman spectroscopy temperature measurements in an internal combustion engine, Opt. Eng. 33 (1994) 2870–2874.
[4] R.W. Dibble, R.E. Hollenbach, Laser Rayleigh thermometry in turbulent flames, in: Proceedings of the 18th Symposium on Combustion, The Combustion Institute, Pittsburgh, 1981, pp. 1489–1499.
[5] C. Chan, J.W. Daily, Measurement of temperature in flames using laser induced fluorescence spectroscopy of OH, Combust. Flame 19 (1980) 1963–1968.
[6] P.V. Farrell, D.L. Hofeldt, Temperature measurement in gases using speckle photography, Appl. Opt. 23 (7) (1984).

[7] G. Rousset, F. Lepoutre, Mesures de diffusivités thermiques par la méthode photoacoustique et par l'effet mirage, Rev. Phys. Appl. 17 (1982) 201–207.
[8] J.C. Mombo-Caristan, L.C. Philippe, M.Y. Perrin, J.P. Martin, Laser beam deviation as a local density probe. Application to supersonic free jets, Exp. Fluids 7 (1989) 303–308.
[9] L. Zhang, J.P. Petit, J. Taine, Mesurements of temperature profiles in gases by laser beam deflection, Rev. Phys. Appl. 24 (1988) 401–410.
[10] F. El Ammouri, J. Taine, Measurements of wall conductive heat flux in turbulent gas flow by laser beam defection, Int. J. Heat Mass Transfer 37 (1994) 1759–1771.
[11] P. Bambang-Teguh, Experimental and theoretical studies of combined radiative and convective transfer for high temperature heat exchangers, in: Taylor, Francis (Eds.), International Heat Transfer Conference, Brighton, UK, 1994, Hemisphere, Washington, DC, pp. 345–349.
[12] C. Herman, E. Kang, A method of quantitative visualisation of complex, unsteady thermofluid processes, in: Fluids Engineering Division Conference, vol. 239, San Diego, 1996, ASME, pp. 143–150.
[13] C. Herman, E. Kang, C. Wetzel, Expanding the applications of holographic interferometry to the quantitative visualization of complex, oscillatory thermofluid processes, Exp. Fluids 24 (1998) 431–446.
[14] F. Mayinger, Modern electronics in image-processing and in physical modelling – a new challenge for optical techniques, in: Taylor, Francis (Eds.), International Heat Transfer Conference, Brighton, UK, 1994, Hemisphere, Washington, DC, pp. 61–79.
[15] F. Mayinger, Advanced optical methods in transient heat transfer and two-phase flow, in: Transport Phenomena in Thermal Enginnering, Begel House, Seoul, Korea, 1993, pp. 10–23.
[16] J.H. Hwang, T.M. Liou, Heat transfer in a rectangular channel with perforated turbulence promoters using holographic interferometry measurement, Int. J. Heat Mass Transfer 38 (1995) 3197–3207.
[17] T. Kreis, Holographic Interferometry: Principles and Methods, vol. 1 of Akademie Verlag Series in Optical Metrology, VCH, New York, 1996.
[18] F. Bdéoui, Effet du rayonnement des gaz sur certaines instabilités thermoconvectives, Thése de doctorat, Ecole Centrale Paris, 1998.
[19] G. Lauriat, Numerical study of the interaction of natural convection with radiation in nongray gases in a narrow vertical cavity, in: Proceedings of the Seventh International Heat Transfer Conference, vol. 2, Munchen, 1982, Hemisphere, Washington, DC, pp. 153–158.
[20] A. Yucel, S. Acharya, M.L. Wiliams, Natural convection and radiation in a square enclosure, Numer. Heat Transfer 15 (1989) 261–278.
[21] T. Fusegi, K. Ishii, B. Farouk, K. Kuwahara, Three-dimensionnal study of convection-radiation interactions in a cubical enclosure fields with a non-gray gas, in: Taylor, Francis (Eds.), Proceedings of the Ninth International Heat Transfer Conference, vol. 6, Jerusalem, 1990, Hemisphere, Washington, DC, pp. 421–426.
[22] A. Draoui, F. Allard, C. Beghein, Numerical analysis of heat transfer by natural convection and radiation in participating fluids enclosed in square cavities, Numer. Heat Transfer A 20 (1991) 251–261.
[23] L. Foucher, J.P. Petit, Numerical simulations of 2D steady laminar convection flows around one or several enclosed thin plates, in: Taylor, Francis (Eds.), Proceedings of the 11th International Heat Transfer Conference, vol. 3, Kgong Ju, Korea, 1998, Hemisphere, Washington, DC, pp. 251–256.
[24] E. Iacona, Application de l'interférométrie holographique à l'étude des transferts thermiques couplés dans un gaz au sein d'une cavité. Essai de modélisation, Thése de doctarat, Ecole Centrale Paris, 2000.
[25] F. Mayinger, W. Panknin, Holography in heat and mass transfer, in: Proceedings of the International Heat Transfer Conference, vol. 6, Tokyo, 1974, pp. 28–43.
[26] M. Born, E. Wolf, in: Priciples of Optics, Pergamon Press, New York, 1980.
[27] K.W. Bench, R.H. Muller, C.W. Tobias, Light-deflection effects in the interferometry of one-dimensional refractive-index fields, J. Opt. Soc. Am. 65 (5) (1973) 559–566.
[28] G.S.G. Beveridge, R.S. Schechter, in: Optimization: Theory and Practice, McGraw-Hill, New York, 1970.
[29] J.-P. Holmann, in: Heat Transfer, McGraw-Hill, New York, 1992.
[30] A. Bejan, in: Heat Transfer, Wiley, New York, 1993.
[31] F. Bdéoui, A. Soufiani, P. Le Quéré, A numerical study of Rayleigh–Benard convection in radiating gases, in: Taylor, Francis (Eds.), Proceedings of the 11th International Heat Transfer Conference, vol. 7, Korea, 1998, Hemisphere, Washington, DC, pp. 261–266.